INTERNATIONAL JOURNAL FOR NUMERICAL METHODS IN FLUIDS
Int. J. Numer. Meth. Fluids 2000; **32**: 29–50

Vortex particle-in-cell method for three-dimensional viscous unbounded flow computations

Chung Ho Liu[a,*] and Denis J. Doorly[b]

[a] *Rotating Fluids and Vortex Dynamics Laboratory, Department of Aeronautical Engineering, Chung Cheng Institute of Technology, Ta-Hsi, Tao-Yuan 335, Taiwan, Republic of China*
[b] *Department of Aeronautics, Imperial College, London SW7 2BY, UK*

SUMMARY

A new vortex particle-in-cell (PIC) method is developed for the computation of three-dimensional unsteady, incompressible viscous flow in an unbounded domain. The method combines the advantages of the Lagrangian particle methods for convection and the use of an Eulerian grid to compute the diffusion and vortex stretching. The velocity boundary conditions used in the method are of Dirichlet-type, and can be calculated using the vorticity field on the grid by the Biot–Savart equation. The present results for the propagation speed of the single vortex ring are in good agreement with the Saffman's model. The applications of the method to the head-on and head-off collisions of the two vortex rings show good agreement with the experimental and numerical literature. Copyright © 2000 John Wiley & Sons, Ltd.

KEY WORDS: particle-in-cell method; viscous unbounded flow; Biot–Savart equation

1. INTRODUCTION

Vortex methods are well suited to the computation of incompressible unsteady flows. The formulation of the equations with vorticity as a principal variable allows a natural decomposition of the flow field into rotation and irrotational regions, which are, in general, quite distinct in external flows. Further, where the rotation region is limited in extent, the particle-based implementations of the vortex formulation allow a compact representation of the field, enabling computational elements to be concentrated automatically in the regions of rapid spatial variation. Most numerical methods for solving three-dimensional viscous flow use a spectral, finite element or finite difference discretization, usually with a fixed Eulerian grid. These techniques may be adapted to solve the vortex form of the equations, as described by, among others, Dacles and Hafez [1]. Alternatively, an essentially Lagrangian method, such as

* Correspondence to: Department of Aeronautical Engineering, Chung Cheng Institute of Technology, Ta-Hsi, Tao-Yuan 335, Taiwan, Republic of China. Fax: +886 3 3908102; e-mail: chliu@cc04.ccit.edu.twhttp://cc04.ccit.edu.tw/~RFVDLab

CCC 0271–2091/2000/010029–22$17.50

Received August 1998
Revised December 1998

the vortex particle and vortex filament methods, or the vortex particle-in-cell (PIC) method, which is a hybrid Eulerian–Lagrangian approach, may be used. Of these, the vortex particle method has long been used to model unsteady flow in the two-dimensional case, particularly since the work of Chorin [2], and three-dimensional extensions have been considered since the 1980s by, among others, Canteloube [3], Knio and Ghoniem [4] and Winckelmans and Leonard [5]. The filament method has proven difficult to extend successfully to viscous three-dimensional flow, and although it is not considered here, reference may be made to Leonard [6,7] and Chorin [8].

The PIC method applied to vortices was originally described by Christiansen [9], and versions have been presented by Graham [10] and others, mostly in two-dimensional cases and using the streamfunction vorticity formulation. The vortex PIC method has some of the advantages of the Lagrangian particle methods for computing convection, while using an Eulerian grid to compute the diffusion and vortex stretching and tilting. The solution procedure can, therefore, take advantage of fast Poisson solvers on regular grids. In relation to the above, the objective of this paper is to develop a three-dimensional vortex PIC method to be used to solve the Navier–Stokes equations written in a velocity–vorticity formulation.

In this paper, the vortex PIC method is applied to the computation of three-dimensional unsteady, incompressible viscous flows in an unbounded domain. Vortex-dominated flows, such as free jets [11] and the far-field wakes of an aircraft [12], are often very complex and are characterized by the deformation of their vortical structures. Thus, understanding the dynamics and the mutual interaction of various types of vortical motions is essential in understanding and possibly controlling fluid motions. Therefore, the vortex ring has been selected as a case study for the application of the present method. Before the behaviour of the vortex ring is studied, the diffusion model of the present method is first tested. Then the propagation velocity of the single vortex ring is compared with Saffman's [13] model and numerical diagnostics in terms of satisfaction of the conservation laws are provided. Finally, the mutual interaction of the two vortex rings is investigated

2. GOVERNING EQUATIONS

In the velocity–vorticity formulation for incompressible flow, using the constrain of $\nabla\cdot\vec{u}=0$ and taking the curl of the equation with the definition of vorticity

$$\vec{\omega}=\nabla\wedge\vec{u}, \tag{1}$$

a Poisson equation is obtained that relates the velocity and vorticity fields,

$$\nabla^2\vec{u}=-\nabla\wedge\vec{\omega}. \tag{2}$$

Taking the curl of the momentum equation gives the transport equation for vorticity

$$\frac{\partial\vec{\omega}}{\partial t}+\vec{u}\cdot\nabla\vec{\omega}=\vec{\omega}\cdot\nabla\vec{u}+\nabla^2\vec{\omega}/Re. \tag{3}$$

The dimensionless variables are written as follows:

$$(x, y, z) = (\bar{x}, \bar{y}, \bar{z})/L_c, \quad (u, v, w) = (\bar{u}, \bar{v}, \bar{w})/U_c, \quad (\omega_x, \omega_y, \omega_z) = (\bar{\omega}_x, \bar{\omega}_y, \bar{\omega}_z)L_c/U_c,$$

$$t = \bar{t}U_c/L_c,$$

where L_c is the characteristic length and U_c is the characteristic velocity of the flow.

For velocity–vorticity formulations, several studies have appeared in the literature, e.g. Dacles and Hafez [1], Fasel [14], Dennis *et al.* [15], Farouk and Fusegi [16], Napolitano and Pascazio [17], Daube [18], Ern and Smooke [19], Guj and Stella [20], and Guevremont and Habashi [21]. Given an initial distribution of vorticity, the evolution of the velocity and vorticity may be computed by solving Equations (2) and (3) subjected to appropriate boundary conditions. Expressing Equation (3) in conservative form is advantageous, since with consistent discretization, it is readily shown that an initial solenoidal vorticity field should remain so. In this work, however, the non-conservative form is used for easy adaptation to the PIC approach.

3. THREE-DIMENSIONAL VORTEX PIC METHOD

The vortex PIC method has been successfully used in two-dimensional steady and unsteady viscous flows for both an internal and an external bounded domain [22,23]. For three-dimensional flows, the vorticity is a vector. This implies that the vorticity may be changed by vortex stretching or diffusion as it moves with the flow and therefore we must track vorticity as well as the particle positions. Leonard [7] used vortex filaments to represent the vortex lines or, alternatively, the use of vortex particles. However, the above-mentioned methods are not suitable for viscous flows. In the following section, a brief outline of the particle method is given for comparison with the present PIC method.

3.1. Particle methods

The first step in applying the method is to sample the initial continuous vorticity field at points α_i to obtain $\omega_0(\alpha_i)$, which represents the discretized vorticity. Equivalently, instead of $\omega(x_i)$ we may consider the vortex strengths $\vec{k}_i$ within the sampled volumes, so that if the sampling is at equal intervals h on a Cartesian mesh, we can represent the vorticity as $\vec{k}(\alpha_i)/h^3$. Introducing Lagrangian co-ordinates $x_i(t)$, where $x_i(0) = \alpha_i$, the convection of vorticity follows from computing the trajectories:

$$\frac{\mathrm{d}}{\mathrm{d}t}\vec{x}_i(\vec{\alpha}_i, t) = \vec{u}(\vec{x}_i(\vec{\alpha}_i, t), t). \tag{4}$$

The velocity $\vec{u}$ on the right-hand side of Equation (4) can be substituted by

$$\vec{u}(\vec{x}, t) = \int K(\vec{x} - \vec{x}')\vec{\omega}(\vec{x}', t)\, \mathrm{d}\vec{x}'. \tag{5}$$

For a three-dimensional case, kernel K can be written in matrix form as

$$K(\vec{x}) = \frac{1}{4\pi|\vec{x}|^3} \begin{bmatrix} 0 & x_3 & -x_2 \\ -x_3 & 0 & x_1 \\ x_2 & -x_1 & 0 \end{bmatrix}. \tag{6}$$

It is customary to desingularize kernel K in Equation (6) by replacing it with a smoothed kernel, K_σ, within a radius for σ of $r = 0$. Alternatively, a smooth function of the integral can be applied to the representation of the vorticity field by convolving the Dirac δ function representation of the sampled vorticity [24]. The particle sample spacing and σ should be such that neighbouring cores overlap. The velocity of a particle or blob of Equation (5) can be desingularized as

$$\vec{u}(\vec{x}_i, t) = \sum_{j \neq i} K_\sigma(\vec{x}_i(t) - \vec{x}_j(t))k_j(t), \tag{7}$$

where $K_\sigma(\vec{x}) = K(\vec{x}) * f_\delta(\vec{x})$, with $K(\vec{x})$ given in Equation (6), where $f_\delta(\vec{x})$ is a smoothing function and equal to unity outside a radius δ. Appropriate choices for $f_\delta(\vec{x})$ are discussed by Winckelmans and Leonard [5] and Hald [25].

The evolution of the vorticity field over a time step then follows by moving the particles and computing changes in strength and/or positions of each particle due to diffusion and stretching/tilting. The vortex stretching/tilting may be computed by treating

$$\frac{\partial\vec{\omega}}{\partial t} = \vec{\omega} \cdot \nabla\vec{u} \tag{8}$$

as a fractional step, either by substituting for $\vec{u}$ from Equation (7) or by computing a local approximation to the Eulerian gradient of $\vec{u}$.

Several procedures have been derived to model viscous diffusion, such as the random walk of Chorin [2] and the deterministic method of Cottet [26]. The consistency and convergence of these schemes is addressed in papers by, among others, Hald [25] and Hou [27].

3.2. The present PIC method

In the present vortex PIC method, an initial vorticity field is discretized as a set of vortex particles, as in the pure Lagrangian methods above. The strength of each particle is projected onto the nodes of a fixed Eulerian mesh, and the contributions summed to find the mesh vorticity. The velocity field is then calculated by solving Equation (2) on the mesh instead of computing the velocity from the Biot–Savart law applied to the set of vortex particles. Thus, the present work combines the mesh-based methods with the particle formulation to form a hybrid method. However, in comparison with the previous pure particle method, the mesh

effectively smoothes the vorticity over a blob approximating the cell dimensions. The projection of the vortex strengths onto the mesh is based on volume interpolation, illustrated in Figure 1 for a vortex particle, k_p, at point P within a cell. For a uniform Cartesian mesh, this particle contributes the fraction V_G/V ($V = \Delta x \cdot \Delta y \cdot \Delta z$ is the volume of a cell) of its strength to node 'G', and the corresponding vorticity contribution is $\omega = k_p \cdot V_G/V^2$. After solving Equation (2), the nodal mesh velocities are interpolated back onto the particles. The diffusion and the stretching/tilting term are computed on the mesh as a fractional step. Where diffusive fluxes cause vorticity to enter a cell not already containing any particles, new particles are created. The basic framework for implementation of the procedure is shown below, where the solution update comprises a sequence of two fractional steps.

3.2.1. The calculations on an Eulerian frame

3.2.1.1. Calculating the velocity. To calculate the velocity field on the grid, the curl of the vorticity field needs to be calculated for internal grid points only and can be obtained simply by using a central difference approximation for the first derivatives. The velocity boundary conditions can be calculated from the vorticity field on the interior grid by using the Biot–Savart law, which is given as follows:

$$\vec{u}(\vec{x}, t) = \sum_{i,j,k} \frac{\vec{\omega}_{i,j,k} \times (\vec{x} - \vec{x}_{i,j,k})}{4\pi |\vec{x} - \vec{x}_{i,j,k}|^3} \cdot h^3. \tag{9}$$

Each grid point has a support of volume h^3, where $h = \Delta x = \Delta y = \Delta z$, for a uniform mesh.

The corresponding interior velocity field is then found from the Poisson equation (2) with the Dirichlet boundary conditions described above. Applying central differencing to Equation (2) gives the usual seven-point discretization of the Laplacian and any of a variety of techniques may be used for the solution. For an evenly spaced grid, a fast procedure is to

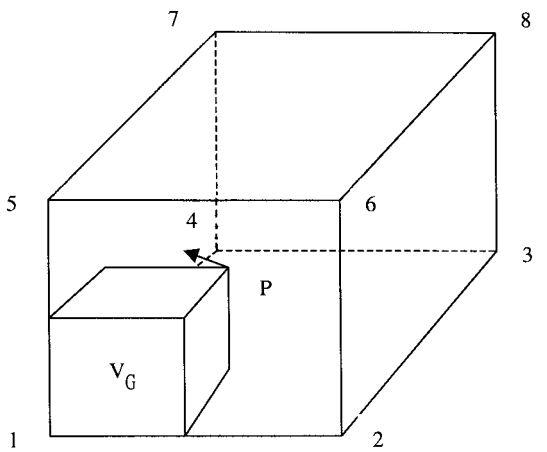

Figure 1. Interpolation of vortex strengths onto mesh vorticity.

Fourier transform the difference equations in two co-ordinate directions, and to solve the remaining one-dimensional system by a tridiagonal solver. For example, letting u denote u_x, by a Fourier sine transformation in streamwise (x) and spanwise (y) directions, one obtains

$$\hat{u}^{k+1}_{m,n} + 2[\cos(\pi m/J) + \cos(\pi n/L) - 3]\hat{u}^{k}_{m,n} + \hat{u}^{k-1}_{m,n} = h^2 \hat{R}^{k}_{m,n}, \tag{10}$$

where the caron symbol denotes a transformed quantity, R is the discretized right-hand side of Equation (2), J and L are the number of mesh points in the x- and y-directions respectively. The solution of Equation (10) followed by an inverse transformation yields u_x; likewise for u_y and u_z.

3.2.1.2. Calculating the vorticity. The vorticity transport equation (3) can be rewritten as

$$\frac{\mathrm{D}\vec{\omega}}{\mathrm{D}t} = \vec{\omega}\cdot\nabla\vec{u} + \nabla^2\vec{\omega}/Re, \tag{11}$$

where $\mathrm{D}\vec{\omega}/\mathrm{D}t$ is the material derivative of the vorticity.

The difference between Equation (3) and Equation (11) is the absence of the convection term $\vec{u}\cdot\nabla\vec{\omega}$ in Equation (11). In the present method, the vorticity is convected explicitly by the moving particles. Thus, the explicit discretization of the convection term that causes smearing of flow features in a purely grid-based method can be avoided. An explicit Euler step is used to update Equation (11) for the vorticity at the next time level.

3.2.2. The calculations on the Lagrangian frame. Having calculated the velocities and vorticities on the mesh points, these results are interpolated back onto the Lagrangian frame to track the particles.

3.2.2.1. Back-projection of the vorticity and velocity and particle moving. The vorticity changes due to diffusion and stretching on the mesh points is interpolated back onto the particles by the same type of bilinear interpolation used for the forward projection. Thus, the new strength of a particle is given by

$$\vec{k}^{n+1}_p = \vec{k}^{n}_p + \sum_{i=1}^{8} \Delta\omega_i \frac{V_i}{V_{ti}} h^3, \tag{12}$$

where h is the cell size and V_{ti} is the sum of the volume contributions V_i from all particles that contribute to the vorticity at node i. The velocity of the particles is also obtained by the same interpolation scheme,

$$\vec{u}_p = \sum_{i=1}^{8} \vec{u}_i \frac{V_i}{V}. \tag{13}$$

The particles are moved by the first-order Euler scheme

$$\vec{x}^{n+1}_p = \vec{x}^{n}_p + \vec{u}^{n}_p \cdot \Delta t. \tag{14}$$

3.3. Outline of the algorithm

3.3.1. Initialization. (1) The initial vorticity is first discretized as a set of particles, $\{\vec{k}_p^0\}$:

$$\vec{\omega}^0 \to \{\vec{k}_p^0\}, \tag{15}$$

then the vorticity strengths of the particles are projected onto the mesh using a volume-based weighting interpolating,

$$\{\vec{k}_p^0\} \to \vec{\omega}_{i,j,k}^0. \tag{16}$$

(2) The velocity components on the mesh are determined by

$$\nabla_D^2 \vec{u}_{i,j,k}^0 = -\nabla_D \wedge \vec{\omega}_{i,j,k}^0, \tag{17}$$

where ∇_D^2 and ∇_D are a discrete approximation to ∇^2 and ∇.

3.3.2. Update. The following sequence advances the flow over one time step:

(3) Interpolate $\vec{u}_p^n$ from $\vec{u}_{i,j,k}^n$ and move particles,

$$\vec{x}_p^{n+1} = \vec{x}_p^n + \vec{u}_p^n(\vec{x}_p) \cdot \Delta t. \tag{18}$$

(4) Project particle strengths onto the mesh vorticity,

$$\vec{\omega}_{i,j,k}^* = P\{\vec{k}_p^n(\vec{x}_p^{n+1})\}. \tag{19}$$

(5) Solve for the diffusion and stretching of vorticity on the mesh,

$$\frac{\vec{\omega}_{i,j,k}^{n+1} - \vec{\omega}_{i,j,k}^*}{\Delta t} = L_D(\vec{\omega}_{i,j,k}^n) + L_S(\vec{\omega}_{i,j,k}^n) = \Delta\vec{\omega}^{n+1}/\Delta t, \tag{20}$$

where L_D and L_S are the discrete diffusion and stretching operators and level * correspond to an intermediate time level.

(6) Back-project the change in nodal vorticity ($B\{\Delta\vec{\omega}\}$) to particles,

$$\{\vec{k}_p^{n+1}(\vec{x}_p^{n+1})\} = \{\vec{k}_p^n(\vec{x}_p^{n+1})\} + B\{\Delta\vec{\omega}_{i,j,k}^{n+1}\}. \tag{21}$$

(7) Create new particles on empty nodes, if the vorticity is larger than the tolerance,

$$\{\vec{k}_p^{n+1}\} \leftarrow \{\vec{k}_p^{n+1}\} \cup \{\vec{k}_p^c\}, \tag{22}$$

where $\vec{k}_p^c$ are newly created particles.

(8) Solve for the velocity field that corresponds to the new vorticity field,

$$\nabla_D^2 \vec{u}_{i,j,k}^{n+1} = -\nabla_D \wedge \vec{\omega}_{i,j,k}^{n+1}. \tag{23}$$

4. NUMERICAL RESULTS

4.1. Validation of the method

(1) The diffusion of an isolated vortex.

We had tested the diffusion scheme for the two-dimensional line vortex [23]. For the three-dimensional flow field, the vorticity distribution is analogous to that of the diffusion of heat from a point source [28].

$$\omega = \frac{\Gamma_0}{8(\pi\nu t)^{1.5}} \exp\left(\frac{-r^2}{4\nu t}\right). \tag{24}$$

In this case, we use the algorithm to compute the (non-physical) diffusion of a single component of vorticity from a point, and compare it with the analytic expression for point diffusion. A uniform mesh of $32 \times 32 \times 32$ cells was used, and the Reynolds number of $Re = \Gamma/\nu = 100$ was considered, where the Reynolds number is defined as the ring circulation (Γ) divided by the kinematic viscosity (ν). The mesh spacings were $\Delta x = \Delta y = \Delta z = 0.1$ and the time step was equal to 0.1. Figure 2 shows the vorticity field for a three-dimensional single vortex particle at different times. From this figure, the present diffusion model is examined and found to match the analytical solution accurately.

(2) The single vortex ring.

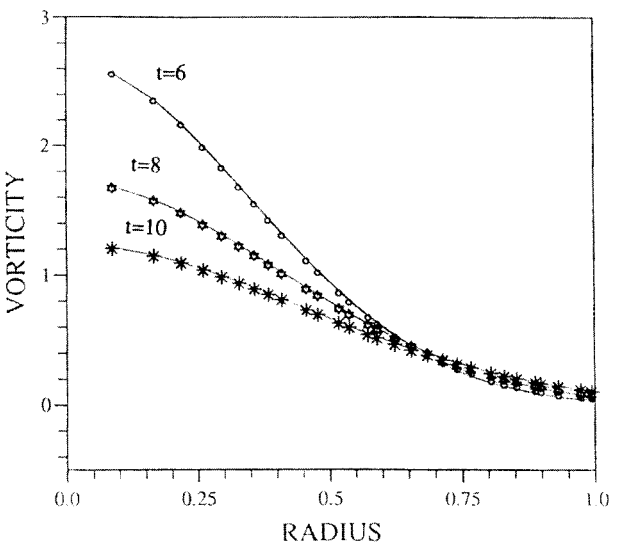

Figure 2. Comparison of the PIC results for diffusion from a three-dimensional point vortex with the analytic solution (line, analytical solution; symbol, present method).

Before we study the mutual interaction of the two vortex rings, we require a simple problem having theoretical results with which to investigate the performance of the present PIC method. The unsteady motion of a single vortex ring in an unbounded viscous flow is selected as a case study to examine the present method. The Kelvin formula for the velocity of a vortex ring of small cross-section with a uniform core vorticity distribution moving in a perfect fluid is given by Lamb [29] as

$$U = \frac{\Gamma}{4\pi R}\left\{\log\frac{8R}{\sigma} - \frac{1}{4}\right\}, \tag{25}$$

where U is the velocity of the vortex ring normal to its plane, R is the radius of the ring, Γ is the circulation and σ is the core radius of the ring. Thus, the propagation velocity of the ring depends on the core radius σ as well as the ring radius R. For a viscous vortex ring, Saffman and Baker [13] accounted for the viscous decay propagation speed by replacing σ by a length scale determined by viscous diffusion. The speed of the viscous vortex ring is given by him as

$$U = \frac{\Gamma}{4\pi R}\left\{\log\frac{8R}{\sqrt{4vt}} - C\right\}, \tag{26}$$

where C is a constant dependent on the vorticity distribution within the core. For a Gaussian vorticity distribution in the core of the ring, the constant C is equal to 0.558. From Equation (26), the effect of viscosity is to slow down the motion of the ring. As we already noted, the propagation velocity depends on the core radius, and Equation (26) accounts for the classical $\sqrt{vt}$ viscous spreading. We will use Equation (26) to compare this with the computational results.

4.1.1. Initial discretization of a vortex ring. The details that are common to all ring computations presented in this paper are given in the following subsection. The co-ordinate system used to describe the ring is shown in Figure 3(a) and (b). The core of the vortex ring is represented by several vortex particles. The vortex ring is thus modelled by a number of vortex particles within its core and forming a vortex torus. The vortex ring is divided into N_s segments of arc length Δs, as shown in Figure 3(a). We obtain $\Delta s = 2\pi R/N_s$. Each of these N_s segments is divided into n_l layers as shown in Figure 3(b). The core structure of the vortex ring is discretized using the same scheme as that used by Winckelmans and Leonard [5]. In this scheme, each vortex particle is allocated part of the total cross-section area normal to the vorticity vector, as shown schematically in Figure 3(b), where, for example, the shaded area equals πr_l^2 with r_l marked. If $n_l = 0$, then one vortex particle is placed at the centre of the circle. If $1 \le n \le n_l$, then additional layers are used with each vortex particle placed at the centroid $r_c = r_l[(1 + 12n^2)/6n]$. Each particle has an equal area πr_l^2 and the radius of the vortex ring core is equal to $\sigma = r_l(2n_l + 1)$. The number of particles per core section is $N_{\text{tot}} = 1 + 4n_l(n_l + 1)$ and the total number of vortex particles are $N_{\text{tot}} = N_s[1 + 4n_l(n_l + 1)]$.

4.1.2. Conservation laws for three-dimensional incompressible unbounded flows. The well-known integral invariants for three-dimensional incompressible unbounded flow are total vorticity $\vec{\Omega}$, linear momentum $\vec{I}$, angular momentum $\vec{A}$, and kinetic energy E. When using a set of vortex particles to represent the flow, these quantities become

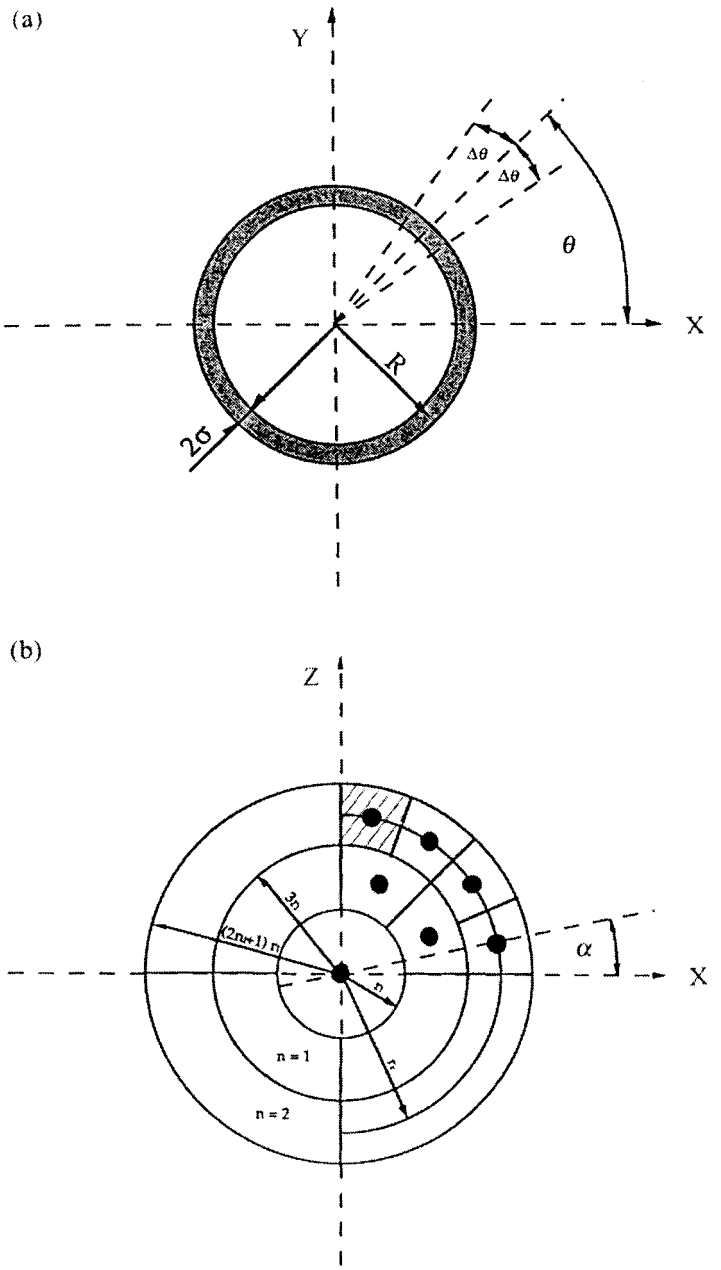

Figure 3. (a) Angular discretization of a vortex ring into sections. (b) Discretization of the ring core.

$$\vec{\Omega} = \sum_p \vec{\kappa}_p(t) = 0, \tag{27}$$

$$\vec{I} = \frac{1}{2} \sum_p \vec{x}_p(t) \wedge \vec{\kappa}_p(t), \tag{28}$$

$$\vec{A} = \frac{1}{2} \sum_p \vec{x}_p(t) \wedge (\vec{x}_p(t) \wedge \vec{\kappa}_p(t)), \tag{29}$$

$$E = \frac{1}{16\pi} \sum_{\substack{p,q \\ p \neq q}} \frac{1}{|\vec{x}_p - \vec{x}_q|} \left(\vec{\kappa}_p \cdot \vec{\kappa}_q + \frac{((\vec{x}_p - \vec{x}_q) \cdot \vec{\kappa}_p)}{|\vec{x}_p - \vec{x}_q|} \frac{((\vec{x}_p - \vec{x}_q) \cdot \vec{\kappa}_q)}{|\vec{x}_p - \vec{x}_q|} \right), \tag{30}$$

where $\vec{\kappa}_p$ is the strength of pth vortex particle. Equation (30) may be integrated directly from $E = \frac{1}{2}\int (\vec{u} \cdot \vec{u})\, \mathrm{d}V$ in the Fourier space [30] or calculated in the physical space [5].

4.1.3. The propagation of a single vortex ring without a core. The first case considered is the computation of the propagation of a single vortex ring without a core. In this model, the cross-section of the ring is represented by one vortex particle with 2000 sections to define the ring. Thus, a total of 2000 vortex particles lie on a single circle of radius $R = 1$. The initial ring centre is placed at $(x_0, y_0, z_0) = (2.5, 2.5, 2.0)$. The Reynolds number for the computation is 1000. The initial circulation of the ring was 1. The time step used was $\Delta t = 0.01$ and a total of 700 time steps were performed. The mesh spacings were $\Delta x = \Delta y = \Delta z = \frac{5}{64}$ and a mesh of $64 \times 64 \times 64$ cells was used. The stretching and diffusion terms of the vorticity transport equation were solved by an explicit finite difference scheme as described above. Far-field velocity boundary conditions are imposed by using the Biot–Savart law with the projected nodal strengths. Since most of the nodal points have zero vorticity in the computational domain, they do not contribute to the velocity field. Therefore, the number of nodes carrying vorticity is much less than the number of particles, so that the calculation of the velocity boundary conditions using the nodal strengths is cheaper than using the particle strengths. Also, since the particles do not approach the boundary too closely, the increase in using the nodal lumped values is small.

The propagation of the single vortex ring without a ring core is shown in Figure 4. The distance between the different stages has been increased artificially to allow for a better graphical representation. A comparison between the numerical predictions of the ring speed with the viscous decay and the analytic solution (26) is shown in Figure 5. The results show the computations are in good agreement with the values evaluated from Saffman's model. Figure 6 shows the diagnostics of the single vortex ring without a core. The linear and angular momentum should be conserved with the PIC method. However, where diffusion is introduced, it is necessary to include a tolerance level to avoid creating too many particles. Therefore, the results show a slight decrease in linear and angular momentum for the test case (of the order of 0.3%). In Figure 6, the kinetic energy is not conserved. Actually, in viscous unbounded flows, the rate of change of kinetic energy can be deduced by taking the dot product of velocity with the momentum equation and integrating over an unbounded volume [5]. Therefore, we can obtain the following equation:

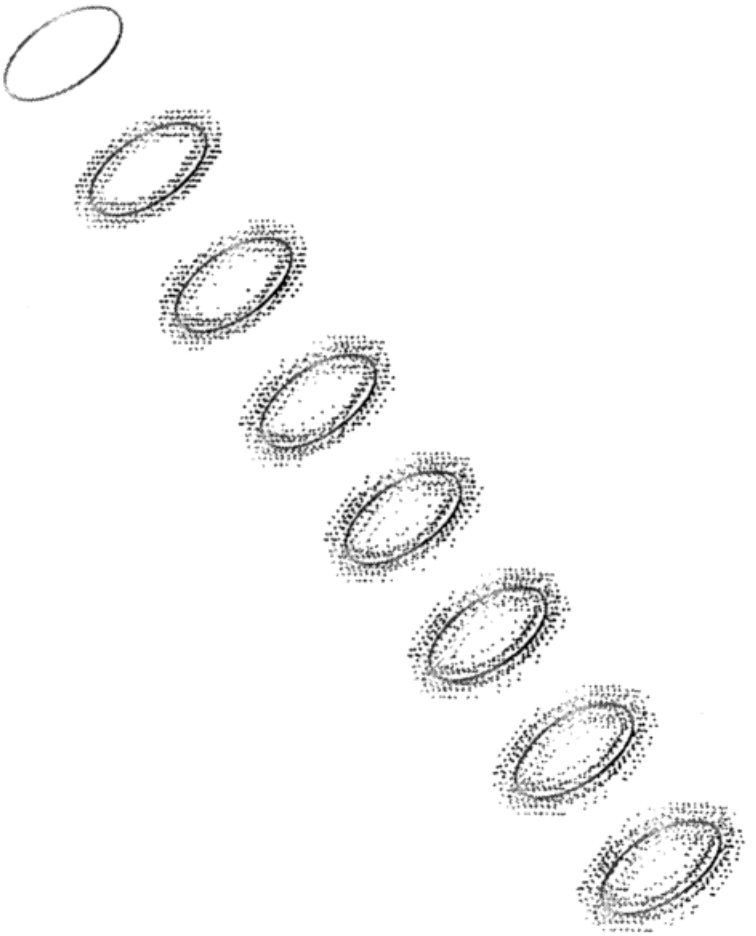

Figure 4. The propagation of a single vortex ring initially without a core from $t = 0$ to $t = 7$ with increments of 1. The plots of vortex particles are ordered top to bottom.

$$\frac{\mathrm{d}E}{\mathrm{d}t} = -\nu\vartheta, \tag{31}$$

where $\vartheta = \int (\vec{\omega} \cdot \vec{\omega})\, \mathrm{d}\vec{x}$ is the enstrophy. Note that due to viscous diffusion, the enstrophy decreases and hence the kinetic energy decreased, either. The enstrophy is not generally conserved in the three-dimensional case or even inviscid flows because of the possibility of vortex stretching.

If we discretized a ring having zero core, it should have infinite velocity according to Equation (25). This is not the case owing to the mesh effect in smoothing the velocity field, which imposes an effective core radius. At $t = 0.01$, the ring velocity from the numerical results

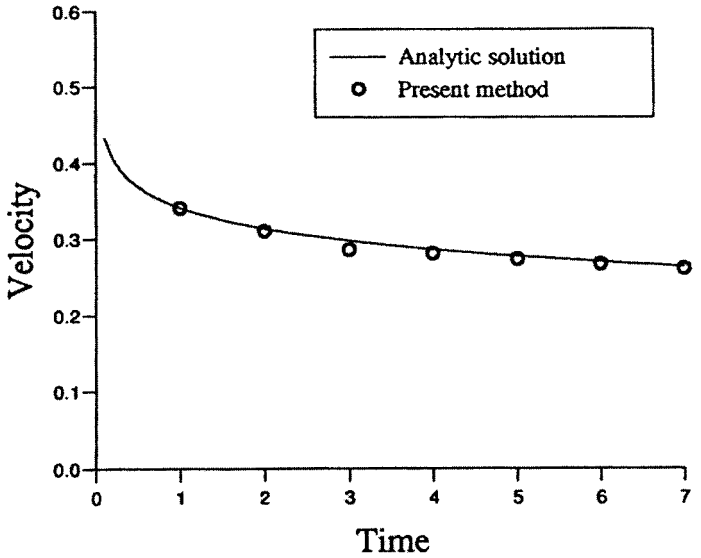

Figure 5. Comparison of the numerical and the analytic results for the speed of evolution of a single vortex ring, initially without a core.

is 0.49. If we substitute $U = 0.49$ into Equation (25), then the 'effective core radius' σ is equal to 0.013. However, if we consider the effect of viscosity, i.e. use Equation (26), then the 'effective core radius' σ is equal to 0.0097. The mesh size used in the simulation was 0.0156, therefore, the mesh radius is 0.0078. Thus, the mesh radius is close to the 'effective core radius' when considering the mesh smearing effect.

4.1.4. The propagation of a single vortex ring with a core. In the second test case of this section, we assign a core size in the above example. The core radius of the ring is 0.1. The Reynolds number, time step, initial ring centre, mesh size and mesh points are the same as for the case in Section 4.1.3. The decay of the propagation speed of the viscous ring is due to the viscous effect, and from Figure 7, the present results are again in good agreement with the results from Saffman's model. The diagnostics of this case are shown in Figure 8. The linear momentum and angular momentum show a slight decrease, as shown in Figure 6. The kinetic energy and entrophy are not conserved. After $t = 2$, the slopes of the decreases of the energy and entrophy become quite flat as the decay tails off with a weaker ring.

The CPU time required for the solution of this case on $64 \times 64 \times 64$ cells for 700 time steps was 3 h on the Digital workstation. Simulations on grids up to $128 \times 128 \times 128$ cells showed that the present numerical solution converges to the analytical solution as the grid is refined.

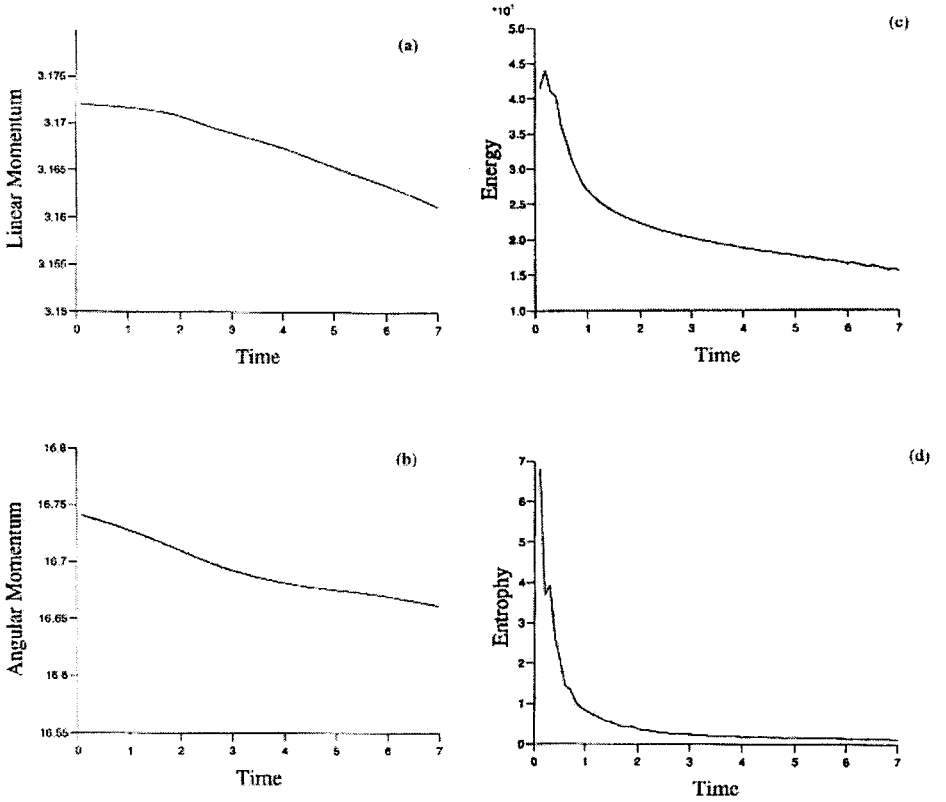

Figure 6. The single vortex ring initially without core: diagnostics (a) linear momentum, (b) angular momentum, (c) kinetic energy, (d) entrophy.

4.2. Application of the method

(1) The head-on collision of two vortex rings.

The collisions of the vortex ring with other rings have provided a wealth of information about vortex dynamics, which is one of the most fundamental means of understanding fluid motion, especially at high Reynolds number and in turbulent flows. In this section, two identical vortex rings with an opposite sense of rotation moving toward each other along a parallel line are studied. The aim of the numerical simulation of the head-on collision of two vortex rings is to mimic the inviscid case of a ring/wall interaction by using an image vortex ring to simulate the effect of the boundary. Since no solid boundary is involved, slip is allowed between the two rings at the plane of collision. In the computation, the ring at $Re = 1000$ was considered. A mesh of $256 \times 256 \times 40$ cells was used with 360 sections to define the ring. The mesh spacings were $\Delta x = \Delta y = \Delta z = 0.00117$. The ring radius is 0.015 and the core radius is 0.003. The time step used was 0.1.

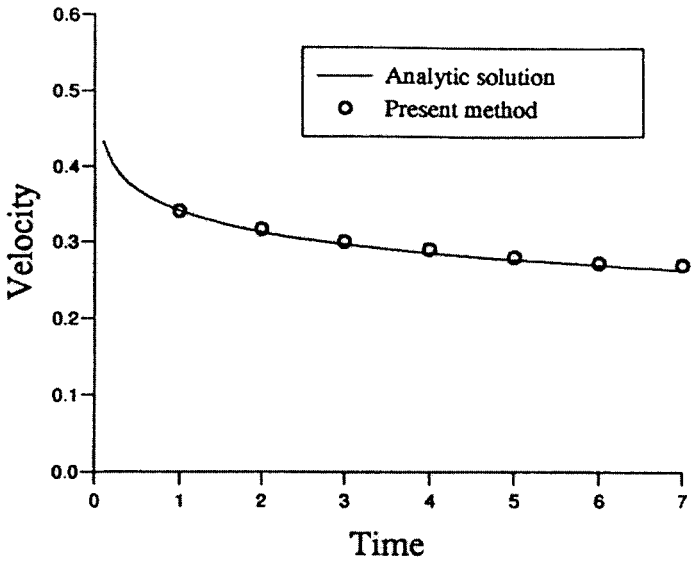

Figure 7. Comparison of the numerical and the analytic results for the speed of evolution of a single vortex ring, initially with a core.

In inviscid flow, the head-on collision of the two vortex rings can be considered as the problem of a single vortex ring moving towards a wall. In the real flow, with a solid wall, the impinging vortex ring induced secondary vorticity, which stops the ring expanding. The evolution of the head-on collision of two vortex rings from $t = 0$–4, with increments of 1, is shown in Figure 9. When two rings approach each other, their diameters increase due to the velocity induced by the other ring. The shape of the ring core deforms from circular ($t = 0$) to a flattened airfoil-like shape as they collide. From Figure 9, the ring diameter expands after collision and no secondary vortex is formed during the collision.

(2) The head-off collision of two vortex rings.

In this case, the collision of two vortex rings with equal strength moving toward one another along a parallel, but off-axis, line is studied. This problem has been studied numerically by Zawadzki and Aref [31], who used vortex-in-cell methods in inviscid flow to study the mixing during vortex ring collision. They also found that the radius of the vortex ring increases during the interaction of the two rings. Only large-scale motion of the vortices was observed in their numerical results. They did not observe the generation of the small-scale ones during the collision of the two rings. Recently, Smith and Wei [32] have presented detailed experimental results identifying small-scale structures arising during off-axis vortex ring collisions. In the present case, we examine whether a simulation using the present vortex PIC method can reproduce more of the features seen in the experiment.

For the numerical simulation, the ring at $Re = 1000$ was considered. Each ring is described by 180 sections, each of 169 particles. Thus, 30420 vortex particles per ring are projected onto

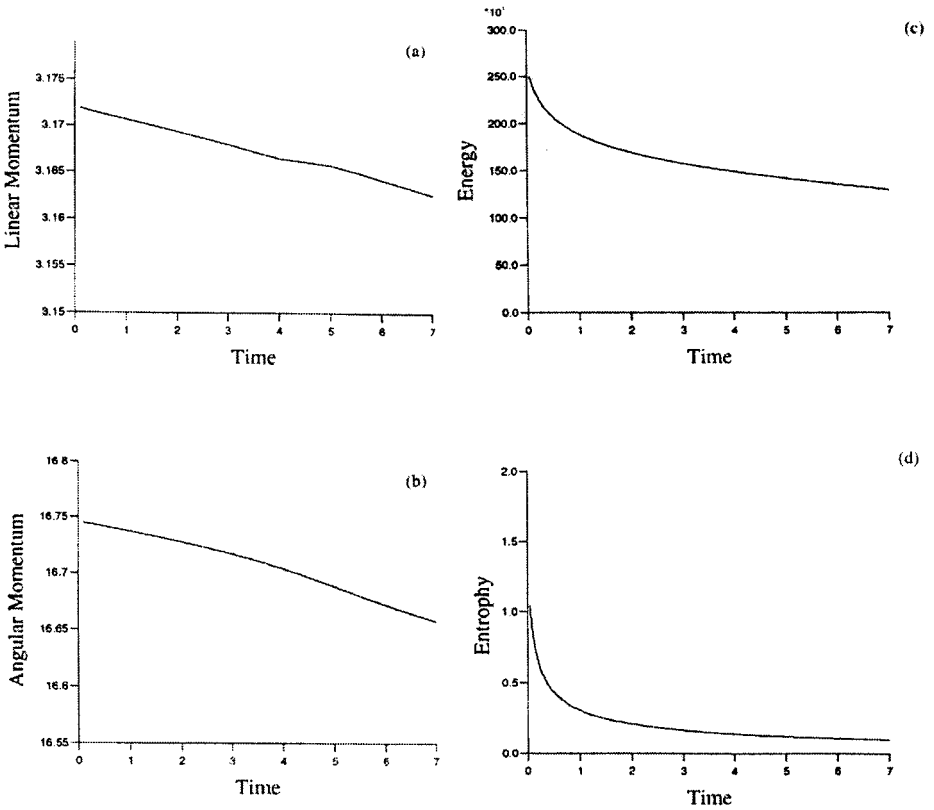

Figure 8. The single vortex ring initially with a core: diagnostics (a) linear momentum, (b) angular momentum, (c) kinetic energy, (d) entrophy.

$128 \times 128 \times 128$ cells. The mesh spacings were $\Delta x = \Delta y = \Delta z = 0.21/128$ and the initial centres of the two rings are placed on (0.111, 0.105, 0.115) and (0.099, 0.015, 0.095) respectively. The ring radius is 0.015 and the ring core is 0.003. The time step used was 0.1. The initial position of the two vortex rings is shown in Figure 10 ($t = 0$). In the present simulation, the two rings moves along the z-direction (i.e. the two rings are offset vertically). The bottom ring moves upward and the top ring downward. The offset of the ring axes (d) is defined as the distance between the centre of the two rings in the x-direction. Then, a dimensionless value, δ, defined as the ratio of the offset of ring axes to the ring diameter, is 0.4 in the present simulation.

4.2.1. Numerical results: large-scale features. When two rings approached closely, the influence of the other ring becomes dominant. In a head-on collision, the two rings move until they touch each other and then they expand axisymmetrically. But, for a head-off collision, the expansion is asymmetrical. Figure 10 shows the sequence of the contour plots of vorticity in the x–z-plane. In this figure, the head-off collision results in the expansion and rotation of the

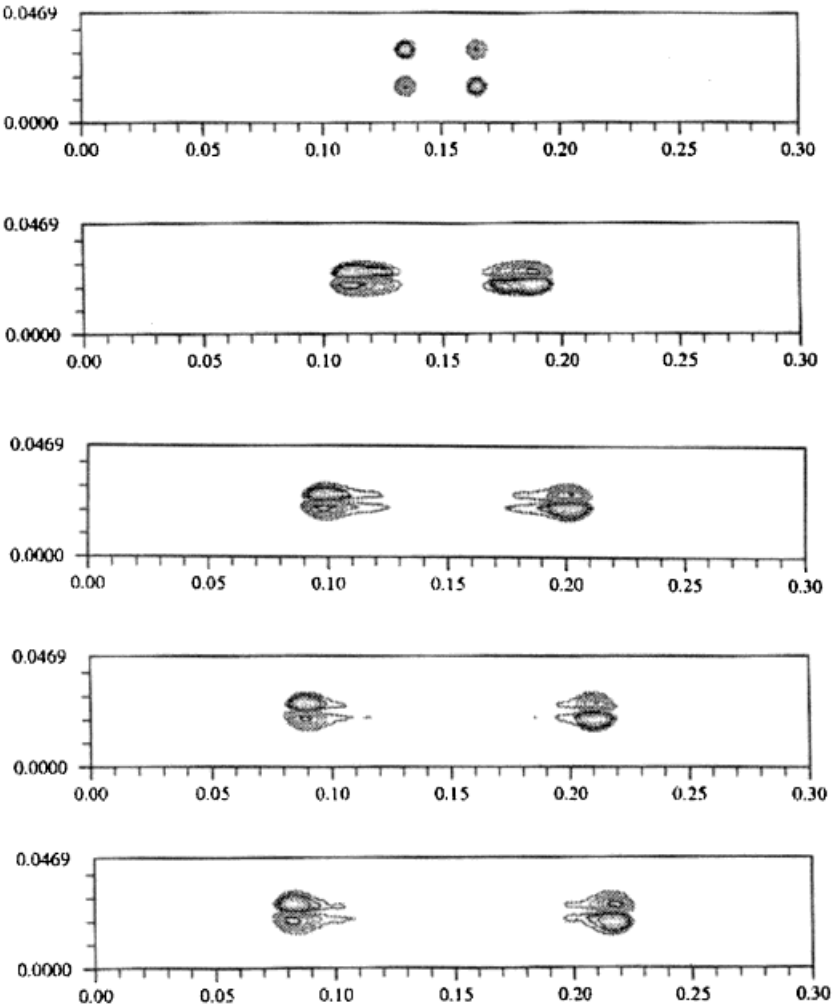

Figure 9. Time sequence for head-on collision of two rings in the x–z-plane from $t = 0$ to $t = 4$ with increments of 1. Contours plots of vorticity are ordered top to bottom.

original rings. This phenomenon is due to the asymmetrical interaction of the two rings. When two rings move next to each other, the 'upper right core' tends to move to the southeast and the 'upper left core' tends to move to the northwest. The 'lower right core' tends to move to the southeast and the 'lower left core' tends to move to the northwest. Therefore, when two rings come in contact with each other, the 'left core pair' tends to move to the northwest and the 'right core pair' tends to move to the southeast. This interaction causes the two rings to rotate and expand. This phenomenon was observed in the previous numerical results [31] as well as in the experimental results [32].

4.2.2. Numerical results: small-scale features. Smith and Wei [32] used a laser-induced fluorescence flow visualization technique to examine the small-scale motions resulting from the collision. In our numerical simulation, the particle visualization for the evolution of the head-off collision of the two rings is shown in Figure 11 ($x-z$-plane) and Figure 12 ($y-z$-plane). Smith and Wei [32] observed a wavy vortex line wrapping around the outside of the primary vortex ring during the interaction of the two rings. In our simulation results (Figures 11 and 12), a wavy phenomenon is observed at $t = 12$. This wavy phenomenon is

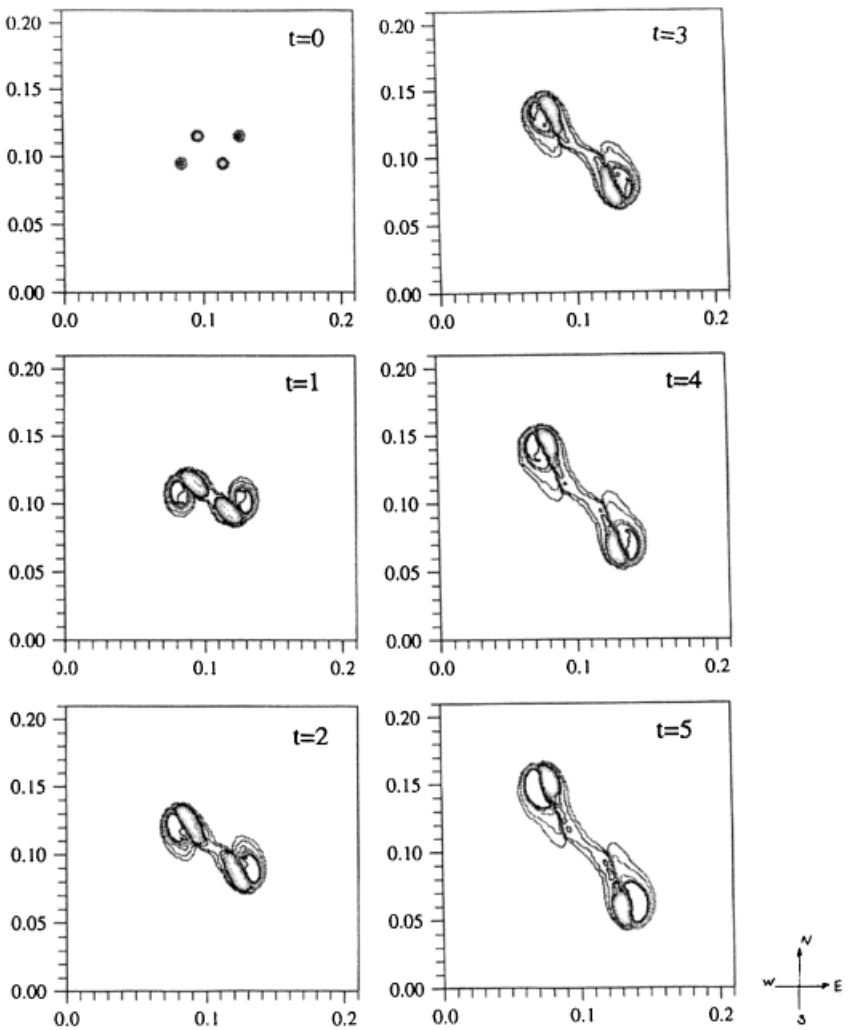

Figure 10. Contour plots of vorticity for the head-off collision of two rings.

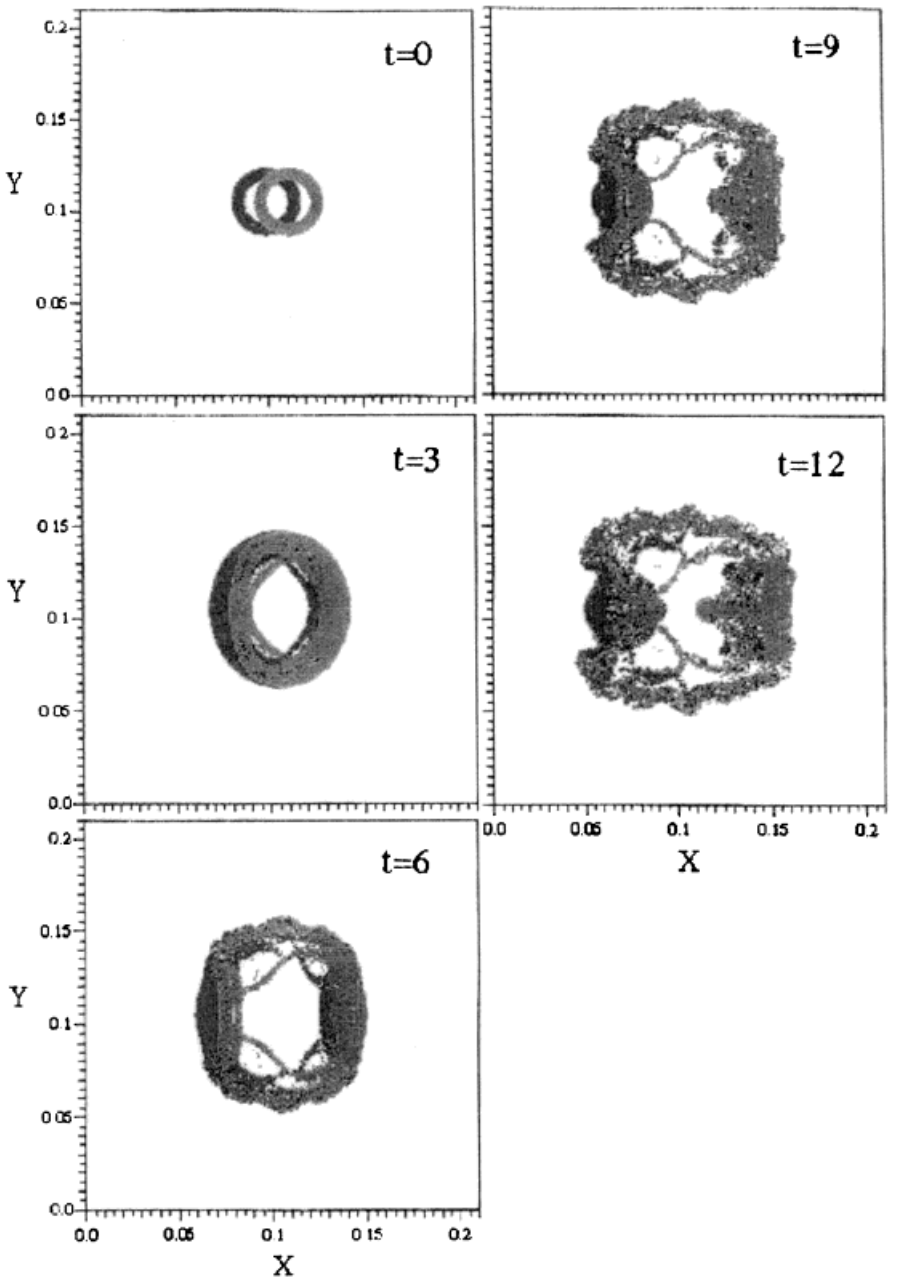

Figure 11. Vortex particle plots for the head-off collision of two rings in the x–y-plane.

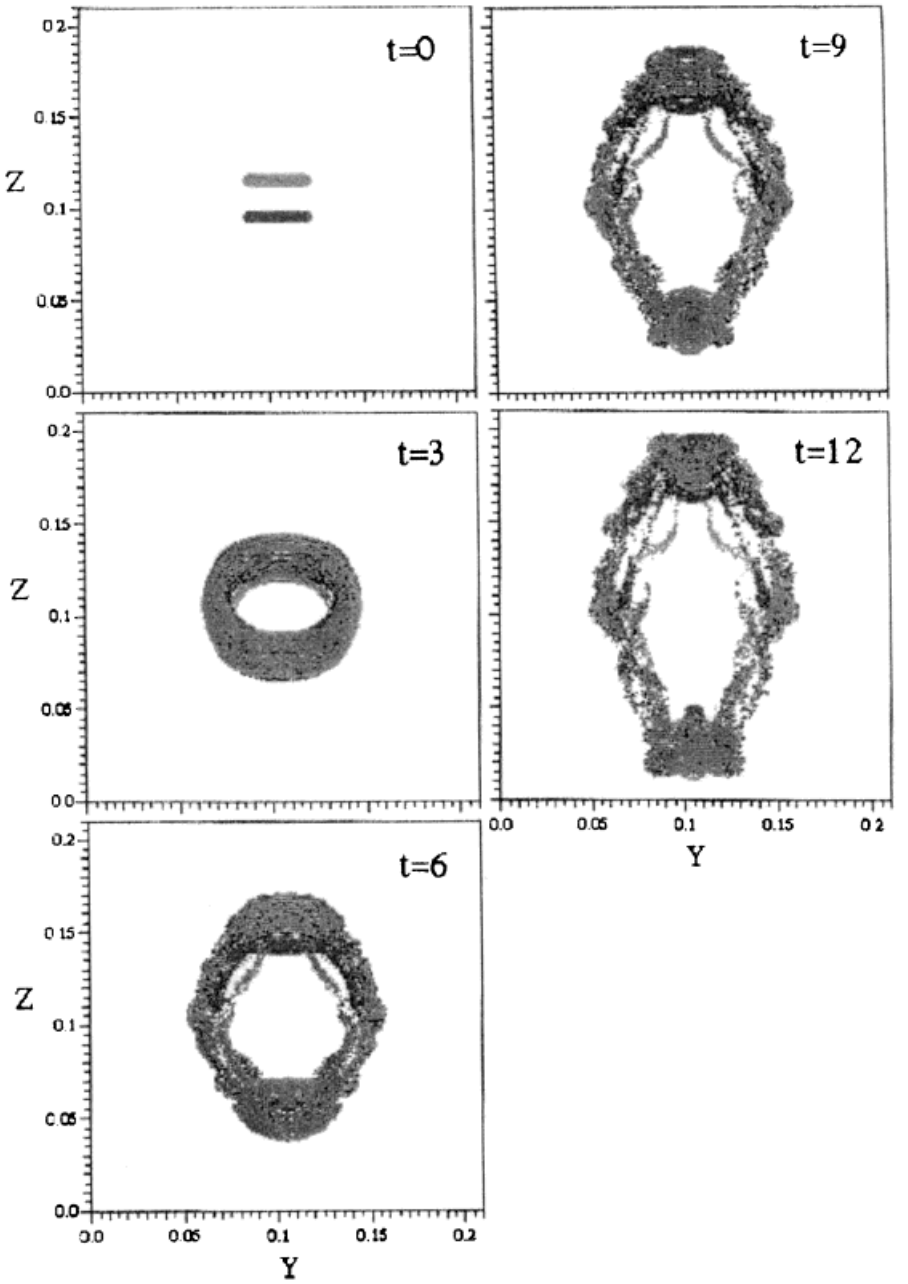

Figure 12. Vortex particle plots for the head-off collision of two rings in the y–z-plane.

caused by the non-uniform vortex stretching of the primary vortex ring. If we look at Figure 11 ($t = 0$), the greatest vortex stretching, as well as the strongest amplification, are at the upper and lower part, which have larger interaction regions than the side part, as mentioned in Figure 1 of Smith and Wei [32].

After $t = 6$, the wavy line becomes more clear and the waviness occurs at the upper and lower part of the interaction region. In the experimental results of Smith and Wei [32], they explained in an idealized sketch that these wavy lines can lead to reorientation of vorticity into counter-rotating ringlets. In Figures 11 and 12, at $t = 9$ and 12, two small ring-like structures can be observed. Although the observation of ringlet formation in the present simulation is not very clear, we do capture the wavy phenomena that could not be shown in the numerical results by Zawadzki and Aref [31].

5. CONCLUSIONS

A new vortex PIC method has been developed for the computation of three-dimensional unsteady, incompressible viscous flows in an unbounded domain. The basic framework for implementation of the procedure has also been introduced, in which the solution update comprises a sequence of two fractional steps. The particle moving is an unconditionally stable procedure, but is subject to an accuracy constraint on the time step. The diffusion and the stretching/tilting operators may be implemented as explicit procedures with corresponding stability limits. A hybrid spectral method, utilizing Fourier transforms in two spatial directions, and a finite difference approximation in the third direction provides a fast solution procedure for the Poisson equation. A non-physical test case, the diffusion of the isolated vortex, was chosen to check the diffusion model in three-dimensional unbounded flows. The results for the propagation speed of the single ring were in good agreement with Saffman's model. The method was applied to three-dimensional unbounded flows, including head-on and head-off collisions of two vortex rings. In these cases, slip was allowed between the two rings at the plane of collision and the results showed no rebounding of the rings after the collision. For the case with head-off collision, the large-scale features of the rings after the collision were in reasonable agreement with the previous experimental and numerical results in the literature. However, the present results showed the development of a wavy-like vortex line wrapping around the primary vortex ring, which was found experimentally but not reproduced in previous numerical studies.

ACKNOWLEDGMENTS

The financial support of this work by the National Science Council of the Republic of China under Grant NSC-87-2212-E-014-020 is greatly appreciated.

REFERENCES

1. J. Dacles and M. Hafez, 'Numerical methods for 3D viscous incompressible flows using a velocity/vorticity formulation', *AIAA Paper 90-0237*, 1990.
2. A.J. Chorin, 'Numerical study of slightly viscous flow', *J. Fluid Mech.*, **57**, 785–796 (1973).

3. B. Canteloube, 'A three-dimensional point vortex method for unsteady incompressible flows', in P. Stow (ed.), *Computational Methods in Aeronautical Fluid Dynamics*, Oxford University Press, Oxford, 1990, pp. 215–248.
4. O. Knio and A.F. Ghoniem, 'Numerical study of a three-dimensional vortex method', *J. Comput. Phys.*, **86**, 75–106 (1990).
5. G.S. Winckelmans and A. Leonard, 'Contributions to vortex particle methods for the computation of three-dimensional incompressible unsteady flows', *J. Comput. Phys.*, **109**, 247–273 (1993).
6. A. Leonard, 'Vortex methods for flow simulation', *J. Comput. Phys.*, **37**, 289–335 (1980).
7. A. Leonard, 'Computing three-dimensional flows with vortex elements', *Annu. Rev. Fluid Mech.*, **17**, 523–559 (1985).
8. A.J. Chorin, 'Hairpin removal in vortex interactions II', *J. Comput. Phys.*, **107**, 1–9 (1993).
9. J.P. Christiansen, 'Numerical simulation of hydrodynamics by the method of point vortices', *J. Comput. Phys.*, **13**, 363–379 (1973).
10. J.M.R. Graham, 'Computation of viscous separated flow using a particle method', in K.W. Morton (Ed.), *Numerical Methods for Fluid Dynamics III*, Oxford University Press, Oxford, 1988, pp. 310–317.
11. J.C. Lasheras, A. Lecuona and P. Rodriguez, 'Three-dimensional vorticity dynamics in the near field of coflowing forced jets', in C. Anderson and C. Greengard (Eds.), *Vortex Dynamics and Vortex Method*, *Lectures in Applied Mathematics 28*, American Mathematical Society, Providence, RI, 1991, pp. 403–422.
12. M. Van Dyke, *An Album of Fluid Motion*, Parabolic Press, Stanford, CA, 1982.
13. P.G. Saffman and G.R. Baker, 'Vortex interactions', *Annu. Rev. Fluid Mech.*, **11**, 95–122 (1970).
14. H. Fasel, 'Investigation of the stability of the boundary layers by a finite difference model of the Navier–Stokes equations', *J. Fluid Mech.*, **78**, 355–383 (1976).
15. S.C.R. Dennis, D.B. Ingham and R.N. Cook, 'Finite difference methods for calculating steady incompressible flows in three-dimensions', *J. Comput. Phys.*, **33**, 325–329 (1979).
16. B. Farouk and T. Fusegi, 'A coupled solution of the vorticity–velocity formulation of the incompressible Navier–Stokes equations', *Int. J. Numer. Methods Fluids*, **5**, 1017–1034 (1985).
17. M. Napolitano and G. Pascazio, 'A numerical method for the vorticity–velocity Navier–Stokes equations in a two and three dimensions', *Comput. Fluids*, **19**, 489–495 (1991).
18. O. Daube, 'Resolution of the 2D Navier–Stokes equations in velocity–vorticity form by means of an influence matrix technique', *J. Comput. Phys.*, **103**, 402–414 (1992).
19. A. Ern and M.D. Smooke, 'Vorticity–velocity formulation for three dimensional steady compressible flows', *J. Comput. Phys.*, **105**, 58–71 (1993).
20. G. Guj and A. Stella, 'A vorticity–velocity method for the numerical solution of 3D incompressible flows', *J. Comput. Phys.*, **106**, 286–298 (1993).
21. G. Guevremont, W.G. Habashi, P.L. Kotiuga and M.M. Hafez, 'Finite element solution of the 3D compressible Navier–Stokes equations by a velocity–vorticity method', *J. Comput. Phys.*, **107**, 176–187 (1993).
22. C.H. Liu and D.J. Doorly, 'Velocity–vorticity formulation with vortex particle-in-cell method for incompressible viscous flow simulation. Part I: formulation and validation', *Numer. Heat Transf. B*, **35**, 251–275 (1999).
23. C.H. Liu and D.J. Doorly, 'Velocity–vorticity formulation with vortex particle-in-cell method for incompressible viscous flow simulation. Part II: application to vortex/wall interactions', *Numer. Heat Transf. B*, **35**, 277–294 (1999).
24. C. Anderson and C. Greengard, 'On vortex methods', *SIAM J. Numer. Anal.*, **22**, 413–440 (1985).
25. O.H. Hald, 'Convergence of vortex method', in K. Gustafasson and J. Sethian (eds.), *Vortex Methods and Vortex Motion*, SIAM, Philadelphia, 1991, pp. 33–58.
26. G.H. Cottet, 'Large time behaviour for deterministic particle approximations to the Navier–Stokes equations', *Math. Comput.*, **56**, 45–60 (1991).
27. T.Y. Hou, 'A survey on convergence analysis for point vortex methods', in C. Anderson and C. Greengard (Eds.), *Vortex Dynamics and Vortex Method*, *Lectures in Applied Mathematics 28*, American Mathematical Society, Providence, RI, 1991, pp. 327–339.
28. H.S. Carslaw, *Conduction of Heat in Solids*, Oxford University Press, London, 1949.
29. H. Lamb, *Hydrodynamics*, 6th edn., Cambridge University Press, Cambridge, 1932.
30. M.J. Aksman, E.A. Nonikov and S.A. Orszag, 'Vorton method in three-dimensional hydrodynamics', *Phys. Rev. Lett.*, **54**, 2410–2413 (1985).
31. I. Zawadzki and H. Aref, 'Mixing during vortex ring collision', *Phys. Fluids A*, **3**, 1405–1410 (1991).
32. G.B. Smith and T. Wei, 'Small-scale structure in colliding off-axis vortex rings', *J. Fluid Mech.*, **259**, 281–229 (1994).

